DFT Modeling of 45S5 and 77S Soda-Lime Phospho-Silicate Glass Surfaces: Clues on Different Bioactivity Mechanism

(Article begins on next page)

28 April 2024

UNIVERSITÀ DEGLI STUDI DI TORINO

1

DFT modeling of 45S5 and 77S soda-lime phospho-silicate glass surfaces: clues on different bioactivity mechanism

Enrico Berardo[1,2], Alfonso Pedone[3], Piero Ugliengo[1], Marta Corno[1,]*

[1]Dipartimento di Chimica, and NIS – Nanostructured Interfaces and Surfaces – Centre of Excellence, Università degli Studi di Torino, via P. Giuria 7, 10125, Torino, Italy

[2]Department of Chemistry, University College London, 20 Gordon Street, WC1H 0AJ, UK

[3]Dipartimento di Scienze Chimiche e Geologiche, Università di Modena e Reggio Emilia, Via G. Campi 183, 41125, Modena, Italy

Keywords. DFT methods; Ab-initio; Molecular-Dynamics simulations; 45S5 Bioglass; surfaces; CRYSTAL code; melt-derived; sol-gel.

*Corresponding author: marta.corno@unito.it

The manuscript was written through contributions of all authors. All authors have given approval to the final version of the manuscript.

Abstract

The reactivity of bioglasses, which is related to the dissolution of cations and orthosilicate groups in the physiological fluid, strongly depends on the key structural features present at the glass surfaces. Based on the composition and the synthetic routes employed to make the glass, surfaces with very different characteristics and thus presenting different mechanisms of dissolution can be observed.

In this paper, the surface structures of two very different bioglass compositions, namely 45S5 (46.1 SiO_2, 24.4 Na_2O, 26.9 CaO and 2.6 P_2O_5 mol %) and 77S (80.0 SiO_2, 16.0 CaO and 4.0 P_2O_5 mol %), have been investigated by means of periodic DFT calculations based on PBE functional and localized Gaussian basis set as encoded in the CRYSTAL code.

Our calculations show that the two glass surfaces differ by the relative amount of key structural sites such as NBOs, exposed ions, orthosilicate units and small rings. We have demonstrated how the number of these sites affects the surface stability and reactivity (bioactivity).

Introduction

Soda-lime silicate glasses with the addition of phosphorus have been widely used in a large number of medical applications since their discovery by Hench and co-workers in the early 1970s.[1]

These melt-quenched phospho-silicate glasses are considered bioactive due to the strong chemical response they induce when implanted in the human body.[2] The bioactive interaction occurs at the glass surface after the immersion in the human blood plasma or in acellular simulated body fluid (SBF) solutions. Indeed, several chemical transformations lead to the growth of a hydroxyl-carbonate apatite (HCA) layer on the glass surface, according to the complex mechanism theorized by Hench.[3,4]

This mechanism consists in five inorganic reaction stages which start as soon as the glass is immersed in physiological fluid. Firstly, the ionic exchange between modifier cations (especially Na^+) and hydronium ions in solution occurs. Then, the glass network is disrupted by the hydrolysis of Si-O-Si bonds which form Si-OH silanol groups. In the third step, the orthosilicic groups previously released in solution condense on the glass surface forming a gel-like surface layer depleted in modifier cations (Na and Ca). Subsequently, an amorphous calcium phosphate layer forms on the gel and it gradually transforms into crystalline hydroxyapatite on which further cellular uptake promote the formation of the bonding interface between the inorganic glass and human hard (bones) or soft (muscles) tissue. Moreover, the just formed layer can activate several genes encoding proteins associated with osteoblast proliferation and differentiation.[3]

Since the rate of glass initial dissolution and HCA crystallization is critical for the bonding ability of the glass, the bioactivity of different compositions is measured in terms of how fast

HCA is formed, *i.e.* more bioactive glasses show faster ion release immediately after contact with the biological medium.[5]

Several features control the biological fixation of these glasses, such as their textural properties (surface area and porosity), particle size and glass composition.[4]

The first generation of bioglasses was obtained by the *melt-quenched* method and the most bioactive one was the renown Hench 45S5 Bioglass (46.1 SiO_2, 24.4 Na_2O, 26.9 CaO and 2.6 P_2O_5 mol %). For these materials, the bioactivity sharply decreased with the increase of silica content, since no HCA deposition was observed for glasses with more than 60% SiO_2.[6] Moreover, the *melt-quenched* method often led to chemically heterogeneous materials, with incipient crystallization and some minor or significant degree of impurities in the actual composition.[7]

In 1991 Li et al.[6] proposed a synthesis of similar bioactive glasses *via* a low temperature sol-gel method, which provides materials with high mesoporosity and high surface area, enhancing the kinetics of HCA formation and expanding the compositional range (up to 90% of silica) for which those materials show bioactive behavior.[5,6] Moreover, because all the steps involved in the sol-gel method are carried out at relatively low temperatures, the addition of components to lower the melting temperature, such as Na_2O, used in the *melt-quenched* route, is no longer required.[7] In this way sol-gel derived bioglasses, such as the 77S (80.0 SiO_2, 16.0 CaO and 4.0 P_2O_5 mol %),[6] showed competitive rates of HCA crystallization compared to the most bioactive *melt-derived* Hench compositions.[5,8-10] In this case, a different mechanism of HCA formation has been proposed after several XRD, FTIR and RAMAN investigations.[4,11,12] It consists in the direct precipitation of the amorphous calcium phosphate layer on the sol-gel glass surface with the reaction kinetics depending on the surface morphology, porosity and silanol concentration.

In the last years an appreciable number of experimental studies have been conducted on bioglasses, using the standard solid-state techniques such as NMR,[13-18] SEM, TEM, DRIFT, XRD,[19-26] RAMAN and infrared spectroscopy[17,30,31] in order to analyze the growth of HCA on their surface. Nevertheless, the complex composition and the amorphous nature of these materials do not allow experiments at an atomistic resolution, which is essential to understand which and how specific structural features affect the rate of HCA deposition.

Nowadays, the continuous advances in theoretical methods and the increasing power in high-performance computers make simulations a convenient alternative to experimental techniques, driving research towards a more fundamental understanding of the properties of these materials. A series of computational methods has shown to be able to provide an unprecedented high resolution view into the atomistic bulk structure and properties of some *melt-quenched* bioglass compositions, such as classical molecular dynamics simulations through the use of both the rigid ionic model[15,27,28] and shell-model,[17,18,29] quantum mechanical Car-Parrinello molecular dynamics simulations[30,31] and energy minimization algorithms included in the CRYSTAL code.[17,27,32-34] Atomistic studies of bioglasses cannot be restricted to the bulk structure only, but simulations must directly focus on the interface itself, revealing how the bulk properties are reflected on the surface of these materials which in turn directly affect their bioactivity.

Previous classical dynamics simulations[35] have compared the dry surfaces of two bioglass compositions, 45S5 and 65S, and suggested a link between substantial sodium amounts in the exposed surface and a more effective bioactive fixation in *melt-derived* soda-lime bioglasses. Recent works showed that the main reason for this behavior is the higher mobility of the sodium ions, which favors the fast superficial dissolution of the glass network.[29,36]

In this work periodic DFT calculations are carried out to investigate the atomistic effects of the absence of sodium on the bioglass structure and how these features are reflected at the surface, by comparing the dry surface of the melt-derived 45S5 Bioglass with that one of the sol-gel 77S Bioglass.

While the computational simulation of glasses by quenching a melt from fuse to room temperature[28,37-39] is a well-established procedure, several issues arise when the structure of a sol-gel prepared glass has to be simulated.[40] A possible approach is to assume these materials to be the same as *melt-quenched* glasses,[41,42] ignoring the specificity of the sol-gel synthesis route. Being the correct simulation of sol-gel glasses an almost impossible task we have ignored the specificity of the sol-gel synthesis route and assumed both compositions quenched from the fuse and studied them with the DFT method (PBE functional and Gaussian basis set as encoded in the CRYSTAL09 computer code). With a state of the art procedure we have generated three different surfaces for both glass compositions and discussed in details their energetics and specific superficial features.

Computational Methods

Glass Generation. For the 45S5 Bioglass model, the periodic unit cell generated in a previous work was considered. The model contains 78 atoms and is characterized by the composition $Na_{12}Ca_7P_2Si_{13}O_{44}$ and by cell size of 10.10 Å (modelled in accordance to the experimental density of 2.72 g/cm^3).[27] Instead, for the 77S Bioglass model we generated a periodic cubic box containing 80 atoms, with composition of $Ca_5P_2Si_{21}O_{52}$ and cell size 10.51 Å (in accordance with the experimental density of 2.389 g/cm^3) by means of *melt-and-quench* classical MD simulations with the GULP package[43] by using an empirical partial charge rigid ionic model.[28,34] Details of

the computational setup and procedures used to obtain the bulk glasses can be found in ref 33 and 34. Although, the system sizes of our models are quite small compared to the extended models employed by Tilocca,[44] previous works suggest that these restricted systems accurately describe fundamental local properties of bioglasses.[33]

Quantum-Mechanical Calculations. After MD modelling, two Bioglass samples (45S5 and 77S) were chosen as starting points for the periodic *ab initio* full geometry relaxation procedure (cell size and internal coordinates), as already described in reference 33. This is a common procedure in the *ab initio* simulation of glasses.[33,45-48] In the present work, all the quantum mechanical calculations performed for 45S5 and 77S Bioglass were run with the *ab initio* CRYSTAL09 code.[32] The Hartree–Fock and the Kohn–Sham Hamiltonians are implemented in CRYSTAL09 for the study of periodic systems. The adoption of CRYSTAL09, which is based on Gaussian basis set (vide infra), allows us to treat 2D systems in a rigorous way, i.e. without the need to resort to an artificial empty gap between periodically repeated slabs in the c direction, as it customarily with plane waves based codes. In the present simulations, the empty space above/below the slab itself extends ad infinitum. All graphical inspections were carried out with the molecular graphics program MOLDRAW and VMD was employed for visualizing the electrostatic potential maps.

Hamiltonian and computational parameters. The General Gradient Approximation (GGA) to density functional theory (DFT), through the PBE exchange-correlation functional, was adopted.[49] The grid of points, over which the interpolation of electronic density and its gradient is performed, was a pruned grid of 75 radial points and 974 angular points, divided into 5 subintervals of 86, 194, 350, 974 and 350 points (keyword XLGRID) resulting in about 1 710 629 grid points for the 45S5 Bioglass and 2 237 250 points for the 77S one. With these grids, the

interpolation of the electron density gives the total number of electrons with an error of 4 x 10^{-4} electrons upon 836 total electrons in the unit cell of the 45S5 Bioglass, while for the 77S the error is of 1 x 10^{-4} electrons upon a total number of 840.

For all calculations the Coulomb and exchange tolerances series were set to 6, 6, 6, 6, 14 standard tolerances (see CRYSTAL09 manual, Ref. 32) which ensure a good accuracy in the calculation of the Fock matrix elements ; the Hamiltonian matrix was diagonalized over 14 *k*-points (shrinking factor IS=3). Internal coordinate optimization was performed via an analytical gradient method, upgrading the numerical Hessian with the Broyden-Fletcher-Goldfarb-Shanno algorithm and selecting the default value for all the needed geometry parameters.

Basis Set. The basis set adopted is an all-electron extended Gaussian-type function (GTF) basis set,[27] which we will label later on as BS1. Na ions are described by a 8-511G basis set with most diffuse shell exponents α_{sp}=0.323 bohr^{-2}. For Ca ion a 86-511(d) basis set has been used with most diffuse shell/polarization exponents α_{sp}=0.295 / α_d=0.3191. Si atoms adopt a 6-21G(d) modified basis set (α_{sp}=0.13 / α_d=0.5), whereas for the P atoms a 85-21G(d) basis set has been employed (α_{sp}=0.135 / α_d=0.74583). Oxygen atoms are described with a 6-31G(d) basis set (α_{sp}=0.2742 / α_d=0.538), while for hydrogen was adopted a 3-1G(p) basis set with α_p=1.100 bohr^{-2} for polarization. The total number of atomic orbitals in the unit cell of the 45S5 Bioglass amounts to 1196 functions, while the 77S unit cell counts 1252 functions.

Results and discussion

This section is organized as follows. Firstly, we briefly introduce the bulk properties of the two different bioglass compositions (45S5 and 77S) in order to assess the fundamental structural changes observed during the surface generation process. The bulk properties of the 45S5

Bioglass were already discussed elsewhere,[17,27,33] while to our knowledge the *ab initio* study of the 77S composition is reported here for the first time. Then, the detailed procedure used to generate surface models is described together with the analysis of obtained results in terms of structure, energetics and electronic properties of these surfaces.

Bulk properties. *45S5 Bioglass* The basic structure of the unit cell (a=9.42 Å, b=10.24 Å, c=10.34 Å, α=88.7°, β=91.7°, γ=86.0°, density 2.82 g/cm^3) is shown in Figure 1a[33] and consists of a random network of distorted SiO$_4$ tetrahedra surrounded by Na$^+$ and Ca^{2+} ions and of two phosphate groups, one isolated and the other linked to a SiO$_4$ group – in Figure 1a labeled (1) and (2), respectively.

Table 1 reports the average bond lengths and angles for the bulk of both bioglasses. In the case of the 45S5 Bioglass, the P-O bond length is 1.57 Å while the Si-O one is 1.63 Å. Likewise, the P-NBO distance of 1.56 Å is smaller than the Si-NBO bond, which is 1.62 Å, and P-BO bonds (1.66 Å) are shorter than Si-BO ones (1.69 Å). These results show that the different strength of T-BO and T-NBO bond (where T=Si, P) is well reproduced by the simulations.[27] The average O-Si-O and O-P-O bond angles are centered at the tetrahedral angle of 109.3° and 109.5°, respectively, while the average Si-O-Si angle is 131.3° and P-O-Si angle is 123.0°. Calcium is coordinated by a number of 6.6 oxygen atoms with an average bond length of 2.42 Å, whereas sodium is surrounded by 5.5 oxygen atoms with average distances of 2.39 Å.

The experimental Na-O bond distances (2.30 and 2.64 ± 0.02 A) reported by Martin. R. A. et al.[50] are in good agreement with data for our 45S5 bioglass bulk model in which both Na-ONBO (2.38 A) and Na-OBO (2.65 A) distances are present. The Na-O coordination number (5.5 with a cutoff distance of 3.3 Å) computed by us is in a good agreement with previous MD simulations by Tilocca[51] which report Na-O coordination numbers between 5.4 and 5.6 oxygen atoms (cutoff

of 3.1 and 3.3 A), while Xiang and Du[52] present a Na-O coordination number of 5.7 (cut off of 3.34 A). Moreover both our values for the Si-O (1.63 A) and P-O (1.57 A) bond distances fit the experimental ones of respectively 1.62 ± 0.02 A and 1.60 ± 0.02 A, and our model (see Table 1) correctly reproduces the experimental range of 2.36-2.72 Å for Ca-OBO and Ca-ONBO observed in the 45S5 Bioglass and in crystalline $Na_2CaSi_2O_6$.[53]

~~Experimental ^{29}Si NMR data[50] suggest that the connectivity of the silicate network is mainly (89%) described by chains of Q2 silicates, while the Q3 species only contribute by 11%. Our values of Q2 (61.5%), Q3 (15.4%) and Q4 (7.7%) differ from the experimental ones, but the trend is the correct one and are in good agreement with the values shown by Tilocca in previous MD simulations[35].~~

77S Bioglass The unit cell of 77S (a=10.00 Å, b=10.60 Å, c=10.34 Å, α=92.4°, β=90.6°, γ=89.5°, density 2.55 g/cm³) is shown in Figure 1b and differs from that of 45S5 due to the absence of Na and to the amount of Si and Ca cations. Also in this model there are two PO_4^{3-}, but one is linked to two SiO_4 groups, while the other is connected to three SiO_4 groups – labeled (1) and (2) in Figure 1b, respectively. The P-O bond length of 1.57 Å is shorter than the Si-O one (1.66 Å). T-BO are smaller than T-NBO, while the average Si-O bond length is longer than the one observed in the 45S5 Bioglass. The average O-Si-O and O-P-O inter-tetrahedral bond angles, of 108.9° and 108.3° respectively, are similar to the 45S5 ones, while the inter-tetrahedral bond angles Si-O-Si and P-O-Si show higher values, which are 142.6° and 135.2°. In the 77S Bioglass composition calcium is 5.6-fold coordinated with average distances of 2.43 Å, thus showing that an increment in the number of BOs in the glass composition causes a variation in the topology of calcium ions coordination shell.

45S5 vs 77S The simultaneous presence of Na and Ca modifier cations in the 45S5 Bioglass structure (SiO_2 48% mol) results in a higher number of NBOs and in a higher network fragmentation; on the other hand the 77S Bioglass (SiO_2 78 % mol) is characterized by a significantly cross-linked Si-O-P network. The analysis of the medium-range structural features such as the Q_n distribution comes in support to what stated above: the 45S5 bulk structure is dominated by chains of Q_2 silicates (61.5%), Q_3 and Q_4 species contribute for a 15.4% and only the 7.7% of the total silicon atoms is Q_1, whereas for the less fragmented 77S bulk structure the 4.8% of the silicon atoms are Q_2, 33.3% are Q_3 and 61.9% are Q_4. In both glass compositions no orthosilicate (Q_0) was found.

Experimental ^{29}Si NMR data provides contradictory results. Martin et al.[50] suggest that the connectivity of the silicate network in the 45s5 bioglass is mainly (89%) described by chains of Q^2 silicates, while the Q^3 species only contribute by 11% whereas a trinomial distribution was proposed by Pedone et al.[17] In the latter case, the host silica matrix consists of chains and rings of Q^2_{Si} (67.2%) SiO_4 tetrahedra cross-linked with Q^3_{Si} (22.3%) species and terminated by a low quantity of Q^1_{Si} (10.1%) species. Our values differ from the results published by Martin but are in better agreement with that by Pedone et al. and are in good agreement with the values shown by Tilocca in previous MD simulations.[35] To the best of our knowledge, no NMR information are available for the 77S glass.

According to previous studies,[44] the Q^n distributions shift to higher *n* values going from the 45S5 to the 77S Bioglass leading to a decrement of the glasses bioactivity. Both simulations and experiments agree with the idea that the presence of a significant fraction of silicate chains is a necessary condition for bioactivity, but that bioactivity is severely inhibited when the silica content is high enough that all chain fragments are fused into rings.[54]

Both 45S5 and 77S compositions reveal an ionic nature as Mulliken net charges are close to the formal ionic charges. For the 45S5 Bioglass the average values are 0.866, 1.534, -2.523 and -2.332 electrons for Na, Ca, $PO_4(1)$ and $PO_4(2)$, while the average values for NBOs and BOs are -0.960 and -0.822 electrons, respectively. For the 77S Bioglass the average values are 1.565, -1.598 and -1.380 electrons for Ca, $PO_4(1)$ and $PO_4(2)$, whereas the average charges for NBOs and BOs are -0.928 and -0.738 electrons. As expected, due to the increased amount of SiO_2, the 77S Bioglass shows a milder ionic behavior compared to Hench's Bioglass. Both glasses reveal a large band gap of 4.4 eV and 4.1 eV for the 45S5 and 77S Bioglasses, respectively, confirming a clear insulating character.

Surface Generation. Starting from the PBE optimized bulk structures, three different slab models have been created for each of the two bioglass compositions (for a total of six surfaces). The slab models were created from the bulk samples through a series of different steps.

First, the optimized bulk structures were cut to model real bi-dimensional surfaces, i.e. periodic along two directions. It is worth to emphasize here that for a real glass no periodicity is expected, neither for the bulk nor for the corresponding surfaces. In our simulations, periodicity is imposed by the adoption of periodic boundary conditions so that the unit cell should be large enough to ensure "randomness" in the atom distribution to mimic the glassy nature of the material. In order to correctly generate the surfaces, the following crucial aspects had to be taken into account: *(i)* the direction of the cut, being in principle an infinite number of possible cuts; *(ii)* the potential dipolarity of the resultant model and *(iii)* the neutrality of the slab unit cell. As point iii) is crucial, we chose the bulk unit cell (neutral) as our minimal block to define our slabs.

Therefore, we defined three different cut defined by (001), (010) and (100) crystal faces, hereafter identified as *ab*, *ac* and *bc* surface models.

The second step accounts for the unfilled valence resulting from the process of surface generation: Si-O and P-O bonds were broken at the surface and we heal all the dandling bonds with oxygens and hydrogens, to restore the proper tetrahedral coordination. Obviously, only the NBOs created with the surface cut were saturated, not those structurally present in the bulk. This approach mimics a chemical process in which water reacts with the freshly cleaved surfaces. This is justified as dissociative chemisorption of water molecules onto the most exposed NBOs and the defective sites like Si_{3c} or P_{3c} is an exergonic process. Furthermore, in the real material the surface is contacting the simulated body fluid (SBF), which excludes the presence of electronic defects at the rings. Therefore in our final slab models there are no Si_{3c} defects, which can be found in differently generated bioglass surface models.[29-31,35]

This procedure has led to three different surfaces for each bioglass (a total of 6 surfaces), which were at first treated by means of molecular mechanics[28] to decrease the dipole moment across the slab before being processed by quantum mechanical optimization (internal coordinates only) at the BS1 level of theory. Figure 2 illustrates the optimized slab geometry for the *ab* surface of the 45S5 Bioglass composition.

Surface relaxation. The main properties of the PBE relaxed surfaces are summarized in Table 2. As a consequence of the reconstruction by H_2O molecules after the cut, the exposed modifier cations such as Na and Ca lose their bulk coordination, and during the optimization process they vary their initial positions in order to restore their bulk environment. This rearrangement is assisted by the deformation of the silicate network and by the movement of the NBOs, some of which protrude out of the surface. The resulting effect of the relaxation process is a slight

decrease in the thickness of the slabs. The surface relaxation also involves a large rearrangement of the exposed hydrogen atoms, which if initially protrude outside the surface, in the relaxed structure tend to interact with adjacent exposed NBOs through H-bonds. In some cases these interactions are strong enough to promote a proton transfer from the original oxygen to a new superficial NBO.

The amorphous nature and the complex connectivity of the studied bioglasses do not allow to completely eliminating the electric dipole across the surfaces (see Table 2). Depending on the cut, the dipole is oriented towards the upper (negative value) or lower face (positive value) of the slab. The highest dipole, in absolute term (-3.706 Debye), is observed for the *bc* surface of the 77S Bioglass, while the lowest one (1.377 Debye) is shown in the 45S5 *bc* surface. These values are, however, small enough to not affect the convergence of the self-consistent process to compute the energy of the systems.

Since all the simulated models show a similar structural behavior, for the sake of brevity we will just comment the specific case of surface *ab* for both glasses.

Figure 3 shows the 45S5 surface model *ab* before and after the relaxation process. The average movement of the Na ions is of 0.45 Å towards the center of the slab*,* while the largest displacement resulted for the Na1 cation (1.83 Å), which increases its coordination number from 3 to 5 during the relaxation. The detail in Figure 4 shows the initial and final coordination of the Na1 ion. The movements of the Ca cations are less pronounced and as they do not show a general trend, we assume that they are directly dependent on the silica network reorganization.

For the less ionic 77S surfaces the lower fragmentation of the silicate network induces during the cut the breaking of more Si-O-Si bonds and consequently a higher BO to OH conversions compared to 45S5 surfaces. This behavior has some effects on the silica rearrangement and to the

displacements of the Ca cations, which are more substantial with respect to the 45S5 surfaces case.

From *ab* surface of 77S glass showed in Figure 5 we observe that the Ca cations of the bottom surface tend to migrate to the upper face (bulk) of the slab, probably influenced by the presence of a dipole of -2.433 Debye in the slab, which is due to the higher concentration of negative charge on that region of the surface. The most prominent rearrangement affects a less exposed Ca ion (Ca1 in Figure 5), which changes its coordination from 6 to 8 oxygen atoms and undergoes a movement of 1.87 Å towards the center of the slab.

Relevant geometrical features of the optimized structures for the *ab* surface of both glasses are listed in Table 1. By the comparison between surface and bulk values it results that the optimization process brings about a lengthening of the average Si-O and P-O bond for both glasses. Also, the average intra-tetrahedral values of O-Si-O and O-P-O angles undergo a slight decrease. The average inter-tetrahedral (Si-O-Si) angle values show a different behavior for the two glasses: for the 45S5 Bioglass it slightly increases from 131.3° to 133.2°, while for the 77S a large drop resulted, from 142.6° to 132.1°. These trends demonstrate the presence (especially in the 77S surfaces) of highly constrained structures like two and three-membered (2M and 3M) rings, which are not observed in the bulk of either 45S5 or 77S glasses.

Orthosilicate species and small rings. Since it is assumed that higher bioactivity levels are usually associated with faster initial network degradation,[5] it is then essential to focus on the surface structural features, which can influence the degradation process.

During the surface generation process, as a consequence of the breaking of Si-O bonds and creation of new NBOs, both glasses tend to decrease their inner connectivity and the relaxed surfaces reveal some species (small rings), which were not present in the bulk materials.

The analysis of the Q_n distribution shown in Table 3 reveals that the surfaces tend to reflect the bulk values rather closely, with an overall shift toward lower n.[35] The 77S *ac* surface tends to expose a small fraction of silicate groups (Q_1), which are linked to the silicate network by just one bond, whereas the 45S5 *ab* and *ac* surfaces present 15 and 7% of orthosilicate group (Q_0) disconnected from the silicate network. Previous works suggested that these orthosilicates can be of critical importance in the acceleration of the degradation process of bioglasses, as they can be directly leached into the contact solution at a low energetic cost, and therefore act as nucleation sites for calcium phosphate precipitation.[9,54] Figure 6 illustrates the Q_0 silicate group exposed on the 45S5 *ab* surface. The orthosilicate tetrahedron is surrounded by network modifier cations and interacts with the silicate network just by H-bond (1.47 Å) through the hydrogen of a surface silanol.

The large rearrangement that bioglasses undergo during the surface relaxation also leads to the surface re-condensation of dandling bonds and the creation of very constrained small rings, which were not originally present in the bulk materials. Table 4 illustrates the different surface density of small rings (2M and 3M) found at the surfaces of the two bioglass compositions. The 45S5 surfaces do not expose any 2M ring on their surface, and a 3M ring can only be found on the *bc* surface. On the contrary, the 77S surfaces reveal a higher surface density of small rings, which all show high geometrical constraints.

Figure 7 illustrates a 2M ring exposed on the 77S *ac* surface. The surface 2M ring shows high geometrical constrain, as the inner angles are $\alpha=78°$ and $\beta=86°$, and the involved silicon atom is five-fold coordinated. Tilocca indeed found small percentages of five-coordinated Si in bulk and slab bioglasses with a low concentration of Na (e.g. 65S).[35] This is supported by ^{29}Si magic angle spinning (MAS) NMR for silicate glasses, at atmospheric pressure, in which a small peak at -150

ppm[55] was attributed to the five-coordinated Si whose peak was previously observed in high pressure samples.[56]

Works led by Tilocca *et al.* showed that the transition from bioactive to bioinactive glass is accompanied by a transformation of the bulk structure from predominantly chainlike to ringlike,[54] which entails that a higher surface density of small rings will characterize the surface of the bioinactive composition.[35] Accurate determination of the energy profiles for the hydrolysis of the silicate structures[30,57] showed that, whereas the internal strain of the 2M ring still makes it thermodynamically favorable, the process is hampered by a kinetic barrier, which has been proved to be twice as high as the one calculated for the same process on pure silica glasses.[58] Nevertheless, it is still not clear how the presence of these rings affect the bioactive process and discussion is still open. Some experimental results[59] suggested that the presence of 3M rings on the surface before soaking does not necessarily lead to bioactivity: instead, they have been proposed to play a key role favoring the calcium phosphate nucleation on the bioglass surface.[35] The above discussion related to both Q_n distribution and the 2M/3M statistics is expected to be model dependent.

Formation Energy for the reconstructed surfaces. For the way in which the present surfaces are defined, the classical definition of the surface energy is not meaningful as we have manually reconstructed the as-cut surfaces by water reaction as in the following equation:

$$Bulk + nH_2O \rightarrow Surface \hspace{2cm} 1$$

where *n* indicates the number of water molecules needed to saturate all the dangling bonds created by cutting the bulk, and *surface* refers to the reconstructed and relaxed surface.

The formation energy measures the energetic cost of replacing bonds occurring in the bulk with bonds derived by reaction with water, to give the final hydroxylated surface. These values do not

measure the reactivity of the final (hydroxylated) surface with respect to its durability when immersed in SBF. Table 2 shows the formation energy per water molecule (E_{form}/H_2O) for all the six slab models. The numbers reported in Table 4 reveal that the 45S5 material is far less prone to form OH groups compared to the ionic interactions enjoyed in the bulk material. The opposite happens for the 77S glass in which the bulk network of Si-O-Si and P-O-Si moieties are replaced by an almost isoenergetic Si-O-H and P-O-H groups at the surface. The formation energies for *ac* and *bc* surfaces are slightly endergonic while, for surface *ab*, the reaction 1 is even favorable (exergonic). These numbers are, obviously, very dependent on the considered model so that some caution is needed to generalize too much the conclusions. We would like to remark here that the reactivity or stability of the systems studied in this manuscript cannot be directly connected to the glass bioactivity, which is a property that depends on very complex mechanism of interactions (see Introduction). Table 4 illustrates the concentration of the relevant sites exposed on the top and bottom layer (3 Å thick) of the surface models. On the one hand, surfaces generated from the Bioglass 45S5, which involve higher formation energy, expose on their top layer a high concentration of NBOs and Na cations, while the concentration of Ca cations is similar for both compositions. The formation energy of 45S5 *ac* surface is the highest (458.4 kJ/mol), consistent with a higher concentration of NBOs and undercoordinated Na cations, and with an average coordination of 3.9 atoms of oxygen. The other two 45S5 surfaces *ab* and *bc* show similar surface concentrations of relevant sites (Table 4) which compare to much similar formation energy.

The less ionic 77S surfaces are all characterized by similar formation energy with similar NBOs concentration, while the presence of exposed Ca cations depends on the specific cut direction. The highest formation energy is for 77S *bc* surface (5.2 kJ/mol), which does not

expose any undercoordinated Ca cation in the top layers. Interestingly, this surface is the least compact one and it is affected by a relatively large dipolar moment (-3.71 Debye) across the surface pointing towards the bottom face of the slab.

Surface hydrophilicity and exposed cations. The surfaces generated from the cut of the two bulk bioglasses also differ, as expected, for the density of surface hydroxylation ($\rho[OH]=$ $n(OH)/nm^2$), as shown in Table 2.

Surface hydroxylation tends to be much higher for the 77S surfaces with values between 4.8 and 6.6, while the 45S5 surfaces show lower surface OH group's density. Our results for the 77S glass are in nice agreement with those reported by Tielens et al. who found a density of 5.8 $n(OH)/nm^2$ for structural models of vitreous silica surfaces containing about 78 atoms.[60]

From the analysis of the average length of the OH bonds (Table 1) a different behavior for the two classes of bioglass surfaces is apparent. The value of the average OH distance in the surface *ab* 77S is 0.98 Å, which is in line with the range between 0.95 and 0.98 Å reported by Tielens[60] for silica surfaces while in the surface *ab* 45S5 is 1.06 Å. This difference can be easily related to the fact that in the composition of the 45S5 bioglass there are both Na and Ca as network modifiers, therefore the generated surfaces will show a more ionic behavior promoting stronger H-bonding interaction between Si-OH with adjacent NBOs.

In order to get a more immediate vision of the surface hydrophilicity we studied the electron iso-density surface color-coded with the PBE electrostatic potential (hereon IDEP) for all of the six slab models generated in this work. In Figure 8 and 9, the most exposed layers of surface *ab* of both compositions are superimposed on their IDEP maps.

The chemical nature of surface sites is predictable when IDEP maps are taken into account. Two varieties of sites can be identified as long as their Lewis acidity/basicity: (i) acidic sites,

represented by the most exposed Na, Ca cations and H atoms (blue zones), (ii) basic sites represented by the silicates and phosphates (red zones). The rough profile of bioglass surfaces does not allow a neat distinction of the two zones, thus it is generally observed a blend of acidic or basic sites with intermediate zones (green).

As already discussed above, the IDEP maps confirm the presence of a dipolar moment in the surfaces e.g. the 45S5 *ab* surface, with a dipole of 2.303 Debye, exposes on the upper face a prevalence of undercoordinated cations (Na and Ca), whereas the lower face shows a predominance of blue zones.

On the upper face of the surface 45S5 *ab* (Figure 8a) the higher concentration of Na cations exceeds the number of negative charges and the overall effect is a red positive zone in the electrostatic potential. The most exposed Na cations are Na1 and Na2, which show a charge of 0.881 electrons, higher than the average one for surface 45S5 *ab* (0.871). Both ions show a low coordination of 4 oxygen atoms. A silicate group with the OH protruding out of the surface is responsible for the blue hump in the IDEP map. Superficial silicates, which counterbalance the positive surface potential generated by the exposed network modified cations, mainly occupy the green zone of the IDEP map. On the lower face of surface 45S5 *ab* (Figure 8b) the overall electrostatic potential is slightly negative, but positive zones are observed in correspondence of surface network modifier cations. Indeed, Na3 and Ca2 show high charges, respectively 0.888 and 1.530 electrons, and low coordination (4 and 5 oxygen atoms) compared to the bulk values (5.5 and 6.6).

For surface 77S *ab* the upper face (Figure 9a) shows an overall negative electrostatic potential, which is only neutralized in correspondence of Ca1 and of the surface silanols, oriented towards the core of the surface, which tend to interact with each other through hydrogen bonding.

Interestingly the Ca1, that shows a coordination of 6 atoms of oxygen, exhibit a Mulliken net charge of 1.544 electrons, which is lower than the average value (1.572). The lower face (Figure 9b) is characterized by a positive overall electrostatic potential, but does not expose any surface Ca cation. The positive contribution can be totally addressed to the orientation of the surface silanols: when the hydrogen of the OH4 is oriented towards the oxygen of the OH5 and the correspondent IDEP map region is green/blue, but when the hydrogen atoms protrude out of the surface (OH5, OH6, OH7) the related regions are blue (positive potential).

Conclusions

In this work we characterized six different surfaces generated from the two bioglasses 45S5 (of composition 46.1 SiO_2, 24.4 Na_2O, 26.9 CaO and 2.6 P_2O_5 mol %) and 77S (of composition 77.8 SiO_2, 18.5 CaO, 3.7 P_2O5 mol %) in the attempt to establish which are the key structural features present at the surface of the two bioactive glasses that could explain the different bioactivity.

The glass structures generated through classical MD using a shell-ion model potential were used as initial guesses for the *ab initio* periodic calculations based on the PBE functional and performed using a Gaussian basis set of double-ζ polarized quality in a periodic fashion as coded in the CRYSTAL09 program.

From the analysis of the bulk we noticed how our simulations reproduce the trend already observed in previous works, where an increasing amount of silica in the glass composition leads to a more interconnected network, dominated by Q_4 species. This increase also affects the electronic properties of the system, e.g. 77S is less ionic and exhibits a lower band gap compared to the 45S5 bioglass.

Different surface cuts of the same bioglass composition reveal different properties, as they are strictly dependent on the type and number of ions exposed on the surface. During the surface relaxation process we observed a significant rearrangement of the glass structure, due to the need of restoring the bulk-like coordination. In the 45S5 surfaces the displacement of the most exposed sodium ions was clearly directed towards the core of the slab, while for the calcium ions were less pronounced and almost in random directions. In the 77S surfaces the calcium ions reveal higher mobility, and the displacement of the ions follows the direction of the dipolar moment across the surface. What we have noticed during our simulations is the consequence of a simple physical effect that is also observed in the relaxation of other ionic surfaces, where after the cut, the exposed ions tend to re-establish their bulk coordination and decrease the electric dipole across the slabs. Our simulations highlight the fundamental importance of the ion coordination, and how the ion microscopic environment affects their mobility.

Recent results from Car-Parrinello and classical MD simulations of Hench Bioglass[29,31,36] suggest that, during the surface generation process, Na ions tend to migrate to the top layers of the surface of the material through a hopping process, where the ion moves in rapid, discrete jumps assisted by the movement of the calcium ions. Our results seem to contradict these recent results, but we have to consider that our models derive from static geometry optimizations, which ignore all the thermally activated processes.

Our calculations show that the surfaces of the two bioactive glasses differ by several aspects, which can be directly related to the different mechanism of the HA formation. The surface of the 45S5 Bioglass presents a higher amount of NBO sites and orthosilicate Q^0 units surrounded by modifier cations. These units are easily dissolved once the glass is in contact with the physiological fluids as expected by the Hench mechanism. On the contrary, the 77S bioglass

surfaces show a higher degree of hydroxylation and a not negligible amount of small rings, which can act as nucleation site for the deposition of the amorphous calcium phosphate layer at the glass surface. The first three steps of the Hench's mechanism, that is the cation/H^+ ion exchange, the loss of soluble silica ($Si(OH)_4$) to solution and the condensation and repolymerization of amorphous SiO_2 surface layer, do not come into play.

Further work is needed to assess the reactivity of 45S5 and 77S Bioglass surfaces and to evaluate how the different surface sites favor or hinder the adsorption of water molecules and the dissolution of the silicate network. In that respect, the evaluation of the accurate electrostatic potential maps can be of great help in docking the water molecule in the most appropriate regions of the surface, where the combination between nucleophilic/electrophilic features may lead to chemisorption.

References

(1)   Hench, L. L. Biomaterials. *Science* **1980**, *208*, 826-831

(2)   Kokubo, T.; Kushitani, H.; Sakka, S. Solutions able to reproduce in vivo surface-structure changes in bioactive glass-ceramic A-W. *J. Biomed. Mater. Res.* **1990**, *24*, 721-734.

(3)   Hench, L. L.; Polak, J. M. Third-generation biomedical materials *Science* **2002**, *295*, 1014.

(4)   Jones, J. R. Review of bioactive glass: From Hench to hybrids. *Acta Biomater.* **2013**, *9*, 4457-4486.

(5)   Arcos, D.; Greenspan, D.; Vallet-Regì, M. A new quantitative method to evaluate the in vitro bioactivity of melt and sol-gel-derived silicate glasses *J. Biomed. Mater. Res.* **2003**, *65A*, 344-351

(6)   Hench, L. L.; Clark, A. E.; Li, R. An investigation of bioactive glass powders by sol-gel processing. *J. Appl. Biomater.* **1991**, *2*, 231-239.

(7)   Siqueira, R. L.; Peitl, O.; Zanotto, E. D. Gel-derived Sio2-Cao-Na2O-P2O5 bioactive powders:synthesis and in vitro bioactivity. *Mater. Sci. Eng. C-Mater. Biol. Appl.* **2011**, *31*, 983-991.

(8)   Hamadouche, M.; Meunier, A.; Greenspan, D. C.; Blanchat, C.; Zhong, J. P. P.; La Torre, G. P.; Sedel, L. Long-term in vivo bioactivity and degradability of bulk sol-gel bioactive glasses *J. Biomed. Mater. Res.* **2001**, *54*, 560-566.

(9)   Cerruti, B.; Magnacca, G.; Bolis, A.; Morterra, C. Characterization of sol-gel bioglasses with the use of simple model systems: a surface-chemistry approach *J. Mater. Chem.* **2003**, *13*, 1279-1286.

(10)   Bonino, F.; Damin, A.; Aina, V.; Miola, M.; Verne, E.; Bretcanu, O.; Bordiga, S.; Zecchina, A.; Morterra, C. In situ Raman study to monitor bioactive glasses reactivity. *J. Raman Spectrosc.* **2008**, *39*, 260-264.

(11)   Pereira, M. M.; Clark, A. E.; Hench, L. L. Calcium phosphate formation on sol-gel-derived bioactive glasses in vitro. *J. Biomed. Mater. Res. Part A* **1994**, *28*, 693-698.

(12)   FitzGerald, V.; Martin, R. A.; Jones, J. R.; Qiu, D.; Wetherall, K. M.; Moss, R. M.; Newport, R. J. Bioactive glass sol-gel foam scaffolds: Evolution of nanoporosity during processing and in situ monitoring of apatite layer formation using small- and wide-angle X-ray scattering. *J. Biomed. Mater. Res., Part A* **2009**, *91A*, 76-83.

(13)   Clayden, N. J.; Pernice, P.; Aronne, A. Multinuclear NMR study of phosphosilicate gels derived from POCl3 and Si(OC2H5)(4) *J. Non-Cryst. Solids.* **2005**, *351*, 195-202.

(14)   Elgayar, I.; Aliev, A. E.; Boccaccini, A. R. Structural analysis of bioactive glasses *J. Non-Cryst. Solids.* **2005**, *351*, 173-183.

(15)   Linati, L.; Lusvardi, G.; Malavasi, G.; Menabue, L.; Menziani, M. C.; Mustarelli, P.; Pedone, A.; Segre, U. Medium-range order in phospho-silicate bioactive glasses: Insights from MAS-NMR spectra, chemical durability experiments and molecular dynamics simulations *J. Non-Cryst. Solids.* **2008**, *354*, 84-89.

(16)   Lockyer, M. W. G.; Holland, D.; Dupree, R. NMR investigation of the structure of some bioactive and related glasses *J. Non-Cryst. Solids.* **1995**, *188*, 207-219.

(17)   Pedone, A.; Charpentier, T.; Malavasi, G.; Menziani, M. C. New Insights into the Atomic Structure of 45S5 Bioglass by Means of Solid-State NMR Spectroscopy and Accurate First-Principles Simulations *Chem. Mater.* **2010**, *22*, 5644-5652.

(18)   Pedone, A.; Charpentier, T.; Menziani, M. C. The structure of fluoride-containing bioactive glasses: new insights from first-principles calculations and solid state NMR spectroscopy. *J. Mater. Chem.* **2012**, *22*, 12599-12608.

(19)   Ogino, M.; Ohuchi, F.; Hench, L. L. Compositional dependence of the formation of calcium-phosphate films on bioglass. *J. Biomed. Mater. Res.* **1980**, *14*, 55-64.

(20)   Kim, C. Y.; Clark, A. E.; Hench, L. L. Compositional dependence of calcium-phosphate layer formation in fluoride bioglasses. *J. Biomed. Mater. Res.* **1992**, *26*, 1147-1161

(21)   Zhong, J. P.; Greenspan, D. C.; Feng, J. W. A microstructural examination of apatite induced by Bioglass((R)) in vitro *J. Mater. Sci-Mater. Med.* **2002**, *13*, 321-326.

(22)   Kokubo, T. Surface-chemistry of bioactive glass-ceramics *J. Non-Cryst. Solids.* **1990**, *120*, 138-151.

(23)   Andersson, O.; Karlsson, H.; Kangasniemi, K. Calcium-phosphate formation at the surface of bioactive glass invivo. *J. Non-Cryst. Solids.* **1990**, *119*, 290-296.

(24)   Branda, F.; Fresa, R.; Costantini, A.; Buri, A. Bioactivity of 1.25CaO center dot SiO2 glass: An FTIR and X-ray study on powdered samples *Biomaterials* **1996**, *17*, 2247-2251.

(25)   Ebisawa, Y.; Kokubo, T.; Ohura, K.; Yamamuro, T. Bioactivity of cao.sio2-based glasses - invitro evaluation. *J. Mater. Sci-Mater. Med.* **1990**, *1*, 239-244.

(26)   Ohtsuki, C.; Kokubo, T.; Ohura, K.; Yamamuro, T. Mechanism of apatite formation on CaO-SiO2-P2O5 glasses in a simulated body-fluid. *J. Non-Cryst. Solids.* **1992**, *143*, 84-92.

(27)   Malavasi, G.; Menziani, M. C.; Pedone, A.; Civalleri, B.; Corno, M.; Ugliengo, P. A computational multiscale strategy to the study of amorphous materials *Theor. Chem. Acc.* **2007**, *117*, 933-942.

(28)   Pedone, A.; Malavasi, G.; Menziani, M. C.; Cormack, A. N.; Segre, U. A new self-consistent empirical interatomic potential model for oxides, silicates, and silica-based glasses *J. Phys. Chem. B* **2006**, *110*, 11780-11795.

(29)   Tilocca, A. Molecular dynamics simulations of a bioactive glass nanoparticle. *J. Mater. Chem.* **2011**, *21*, 12660-12667.

(30)   Tilocca, A.; Cormack, A. N. Exploring the surface of bioactive glasses: Water adsorption and reactivity. *J. Phys. Chem. C* **2008**, *112*, 11936-11945.

(31)   Tilocca, A.; Cormack, A. N. Modeling the Water-Bioglass Interface by Ab Initio Molecular Dynamics Simulations. *ACS Appl. Mater. Interfaces* **2009**, *1*, 1324-1333.

(32)   Dovesi, R.; Saunders, V. R.; Roetti, C.; Orlando, R.; Zicovich-Wilson, C. M.; Pascale, F.; Civalleri, B.; Doll, K.; Harrison, N. M.; Bush, I. J.; D' Arco, P.; Llunell, M. *CRYSTAL09*; Università di Torino: Torino, 2009.

(33)   Corno, M.; Pedone, A.; Dovesi, R.; Ugliengo, P. B3LYP simulation of the full vibrational spectrum of 45S5 bioactive silicate glass compared to nu-silica *Chem. Mater.* **2008**, *20*, 5610-5621.

(34)   Corno, M.; Pedone, A. Vibrational features of phospho-silicate glasses: Periodic B3LYP simulations. *Chem. Phys. Lett.* **2009**, *476*, 218-222.

(35)   Tilocca, A.; Cormack, A. N. Surface Signatures of Bioactivity: MD Simulations of 45S and 65S Silicate Glasses. *Langmuir* **2009**, *26*, 545-551.

(36)   Tilocca, A. Sodium migration pathways in multicomponent silicate glasses: Car-Parrinello molecular dynamics simulations *J. Chem. Phys.* **2010**, *133*.

(37)   Huff, N. T.; Demiralp, E.; Cagin, T.; Goddard, W. A. Factors affecting molecular dynamics simulated vitreous silica structures. *J. Non-Cryst. Solids.* **1999**, *253*, 133-142.

(38)   Vollmayr, K.; Kob, W.; Binder, K. Cooling-rate effects in amorphous silica: A computer-simulation study. *Phys. Rev. B* **1996**, *54*, 15808-15827.

(39)   Lee, B. M.; Baik, H. K.; Seong, B. S.; Munetoh, S.; Motooka, T. Generation of glass SiO2 structures by various cooling rates: A molecular-dynamics study. *Comput. Mater. Sci.* **2006**, *37*, 203-208.

(40)   Malavasi, G.; Menabue, L.; Menziani, M. C.; Pedone, A.; Salinas, A.; Vallet-Regì, M. New insights into the bioactivity of SiO2–CaO and SiO2–CaO–P2O5 sol–gel glasses by molecular dynamics simulations. *J. Sol-gel Sci. Technol.* **2011**, 1-12.

(41)   Petkov, V.; Holzhuter, G.; Troge, U.; Gerber, T.; Himmel, B. Atomic-scale structure of amorphous TiO2 by electron, x-ray diffraction and reverse Monte Carlo simulations. *J. Non-Cryst. Solids.* **1998**, *231*, 17-30.

(42)   Bhattacharya, S.; Kieffer, J. Molecular dynamics simulation study of growth regimes during polycondensation,of silicic acid: From silica nanoparticles to porous gels. *J. Phys. Chem. C* **2008**, *112*, 1764-1771.

(43)   Gale, J. D.; Rohl, A. L. The General Utility Lattice Program (GULP). *Mol. Simul.* **2003**, *29*, 291-341.

(44)   Tilocca, A.; Cormack, A. N. Structural effects of phosphorus inclusion in bioactive silicate glasses. *J. Phys. Chem. B* **2007**, *111*, 14256-14264.

(45)   Tilocca, A.; de Leeuw, N. H. Ab initio molecular dynamics study of 45S5 bioactive silicate glass *J. Phys. Chem. B* **2006**, *110*, 25810-25816.

(46)   Donadio, D.; Bernasconi, M.; Tassone, F. Photoelasticity of sodium silicate glass from first principles. *Phys. Rev. B* **2004**, *70*.

(47)   Ispas, S.; Benoit, M.; Jund, P.; Jullien, R. Structural and electronic properties of the sodium tetrasilicate glass $Na_2Si_4O_9$ from classical and *ab initio* molecular dynamics simulations. *Phys. Rev. B* **2001**, *64*, 214206.

(48)   Van Ginhoven, R. M.; Jonsson, H.; Corrales, L. R. Silica glass structure generation for ab initio calculations using small samples of amorphous silica. *Phys. Rev. B* **2005**, *71*.

(49)   Perdew, J. P.; Burke, K.; Ernzerhof, M. Generalized gradient approximation made simple. *Phys. Rev. Lett.* **1996**, *77*, 3865-3868.

(50)   Martin, R. A.; Twyman, H. L.; Rees, G. J.; Smith, J. M.; Barney, E. R.; Smith, M. E.; Hanna, J. V.; Newport, R. J. A structural investigation of the alkali metal site distribution within bioactive glass using neutron diffraction and multinuclear solid state NMR. *Phys. Chem. Chem. Phys.* **2012**, *14*, 12105-12113.

(51)   Tilocca, A.; de Leeuw, N. H.; Cormack, A. N. Shell-model molecular dynamics calculations of modified silicate glasses. *Phys. Rev. B* **2006**, *73*.

(52)   Xiang, Y.; Du, J. Effect of Strontium Substitution on the Structure of 45S5 Bioglasses. *Chem. Mater.* **2011**, *23*, 2703-2717.

(53)   Ohsato, H.; Maki, I.; Takeuchi, Y. Structure of Na2CaSi2O6. *Acta Crystallogr., Sect. C: Cryst. Struct. Commun.* **1985**, *41*.

(54)   Tilocca, A. Structural models of bioactive glasses from molecular dynamics simulations. *Proc. R. Soc. A* **2009**, *465*, 1003-1027.

(55)   Stebbins, J. F. NMR evidence for five-coordinated silicon in a silicate glass at atmospheric pressure. *Nature* **1991**, *351*, 638-639.

(56)   Stebbins, J. F.; McMillan, P. Five- and six-coordinated Si in $K_2Si_4O_9$ glass quenched from 1.9 GPa and 1200°C. *Am. Miner.* **1989**, *74*, 965-968.

(57) Cho, S. B.; Miyaji, F.; Kokubo, T.; Nakanishi, K.; Soga, N.; Nakamura, T. Apatite-forming ability of silicate ion dissolved from silica gels. *J. Biomed. Mater. Res.* **1996**, *32*, 375-381.

(58) Rimola, A.; Ugliengo, P. A quantum mechanical study of the reactivity of (SiO)2-defective silica surfaces. *J. Chem. Phys.* **2008**, *128*, 204702.

(59) Cho, S. B.; Nakanishi, K.; Kokubo, T.; Soga, N.; Ohtsuki, C.; Nakamura, T. Apatite formation on silica gel in simulated body fluid: Its dependence on structures of silica gels prepared in different media. *J. Biomed. Mater. Res.* **1996**, *33*, 145-151.

(60) Tielens, F.; Gervais, C.; Lambert, J.-F.; Mauri, F.; Costa, D. Ab Initio Study of the Hydroxylated Surface of Amorphous Silica: a New Model. *Chem. Mater.* **2008**, *20*, 3336-3344.

Figure Captions

Figure 1. View along the c axis of (a) Hench 45S5 Bioglass (78 atoms in the unit cell $Na_{12}Ca_7P_2Si_{13}O_{44}$), and (b) 77S Bioglass (80 atoms in the unit cell $Ca_5P_2Si_{21}O_{52}$) optimized unit cells.

Figure 2. View along the *b* axis of the *ab* slab model from 45S5 glass. The blue borders define the orthorhombic periodic cell employed in the calculations. Color codes are: red (O), ochre (Si), yellow (P), magenta (Na), green (Ca), grey (H). The *z* axis identifies the non-periodic direction.

Figure 3. View along the *b* axis of the *ab* slab model from 45S5 bulk before (a) and after the geometry optimization (b). The Na ions that exhibit the highest displacements are encircled by a black broken line, while the arrow shows the directions and the length of the displacement. Na1 shows the largest displacement (1.83 Å).

Figure 4. Detail of the coordination environment for the central Na1 ion, before (a) and after (b) the relaxation process. The chosen coordination radius is of 3.3 Å. All distances are in Å.

Figure 5. View along the *b* axis of the *ab* 77S surface before (a) and after the geometry optimization (b). Ca1 shows the highest displacement (1.87 Å).

Figure 6. Isolated orthosilicate group (encircled in yellow) exposed on the surface 45S5 *ab*. The SiO_4 tetrahedron is interacting with the network through a 1.47 Å H-bond.

Figure 7. 2M ring exposed on *ac* surface 77S. All distances are in Å.

Figure 8. View along the non-periodic direction of surface 45S5 *ab* (a) top, (b) bottom, superimposed with the IDEP (isodensity 10^{-6} electrons, electrostatic potential between -0.02 and +0.02 Hartree). Only the most exposed atoms have been superimposed to the IDEP map.
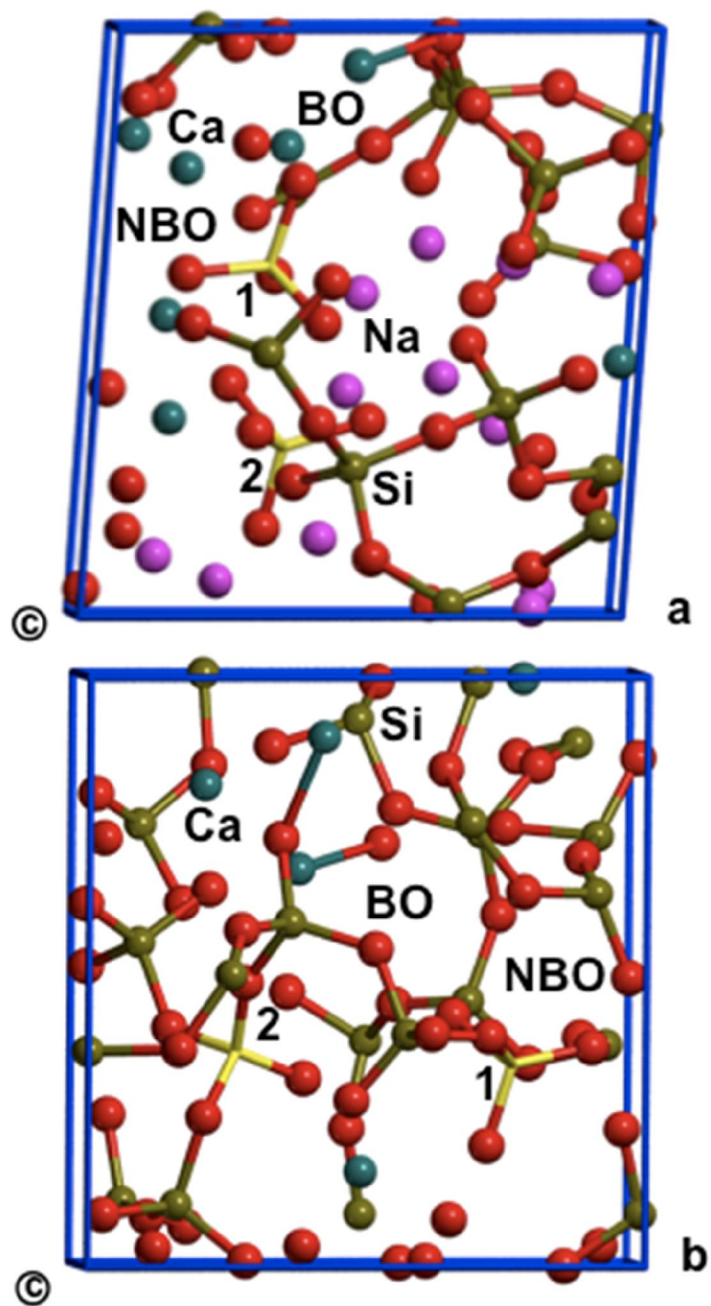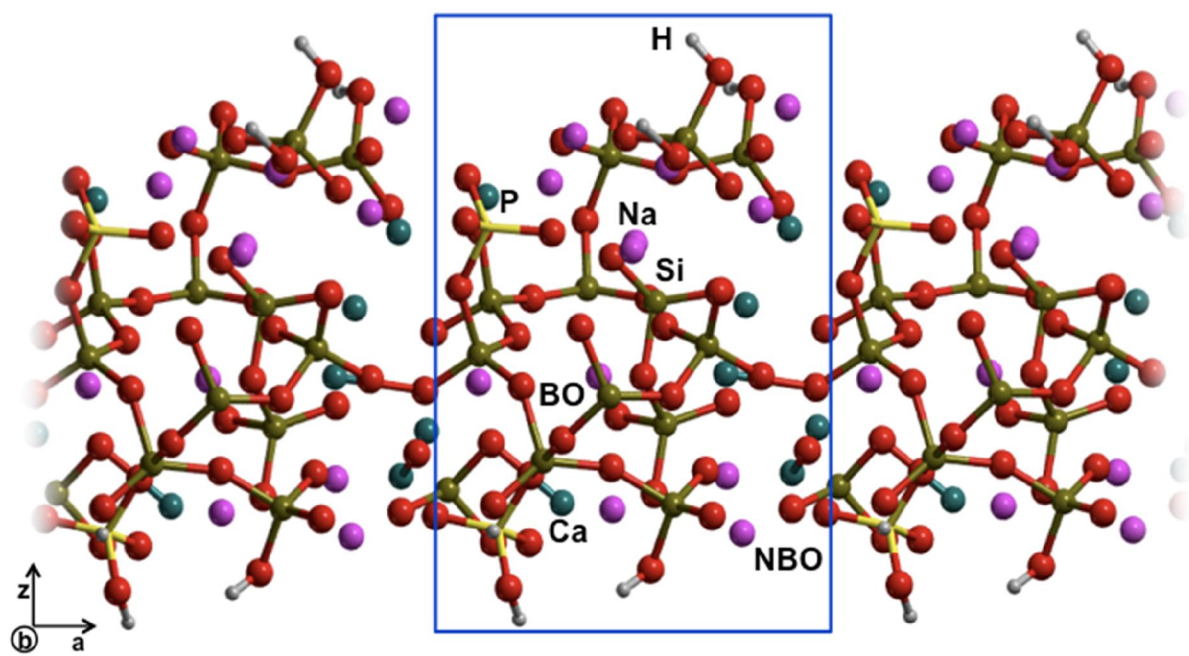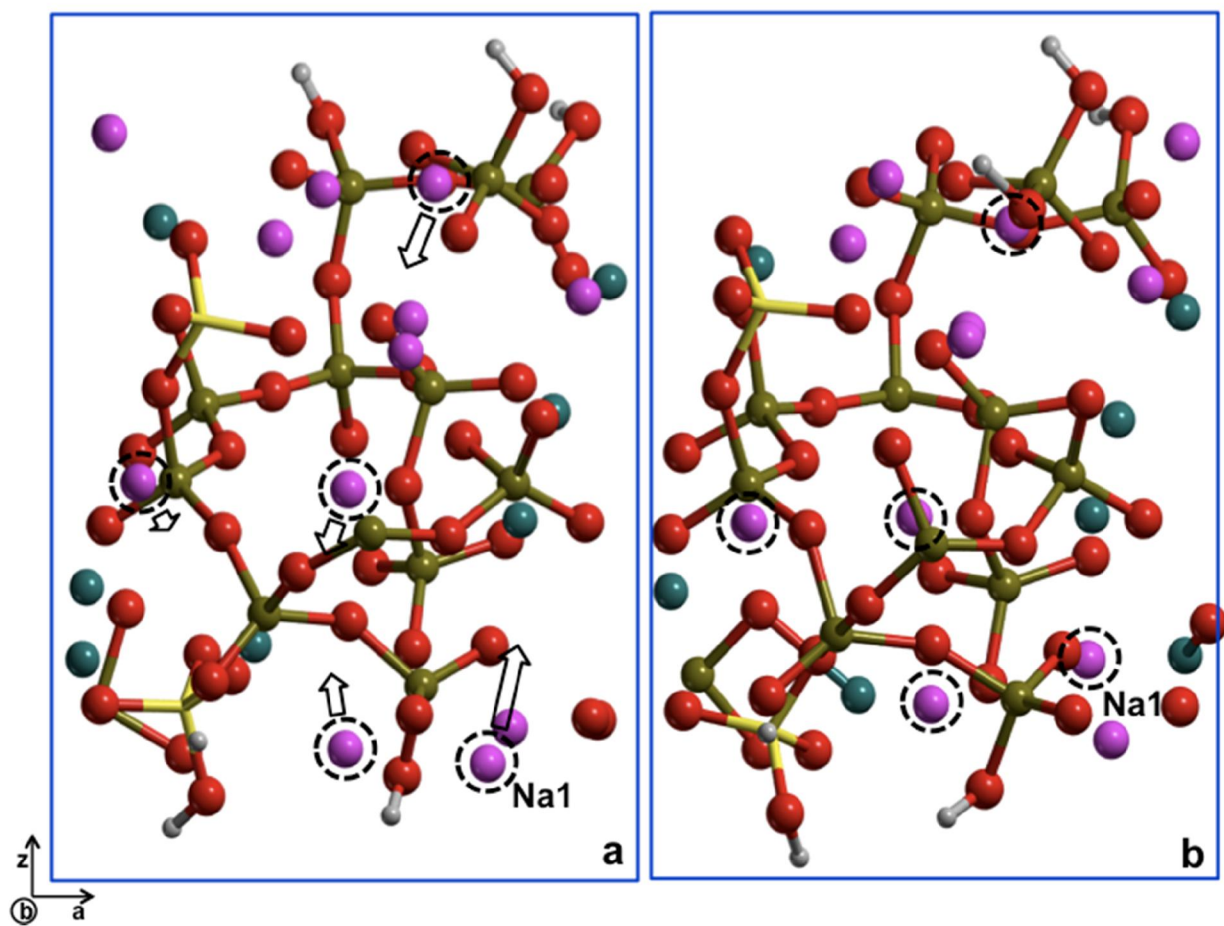
Figure 9. View along the non-periodic direction of surface 77S *ab*, (a) top, (b) bottom, superimposed with the IDEP (isodensity 10^{-6} electrons, electrostatic potential between -0.02 and +0.02 Hartree). Only the most exposed atoms have been superimposed to the IDEP map.

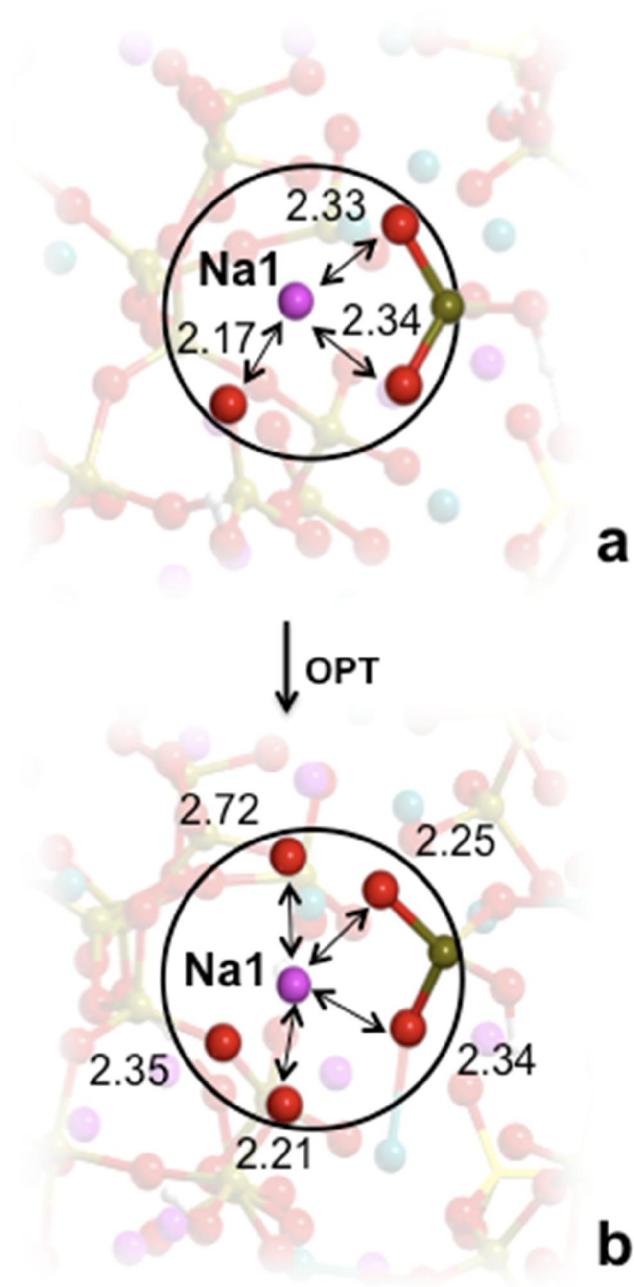**Figures**

Figure 1.

Figure 2.

Figure 3.

Figure 4.
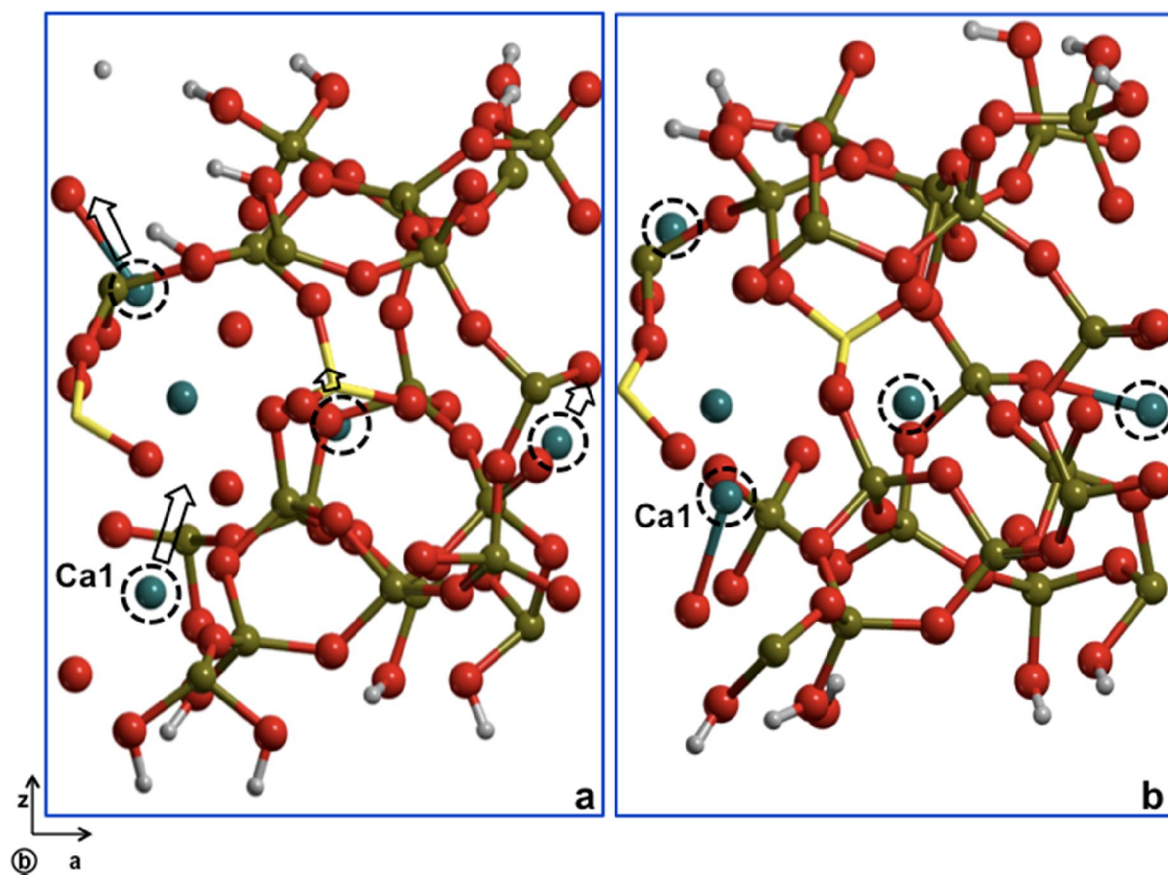
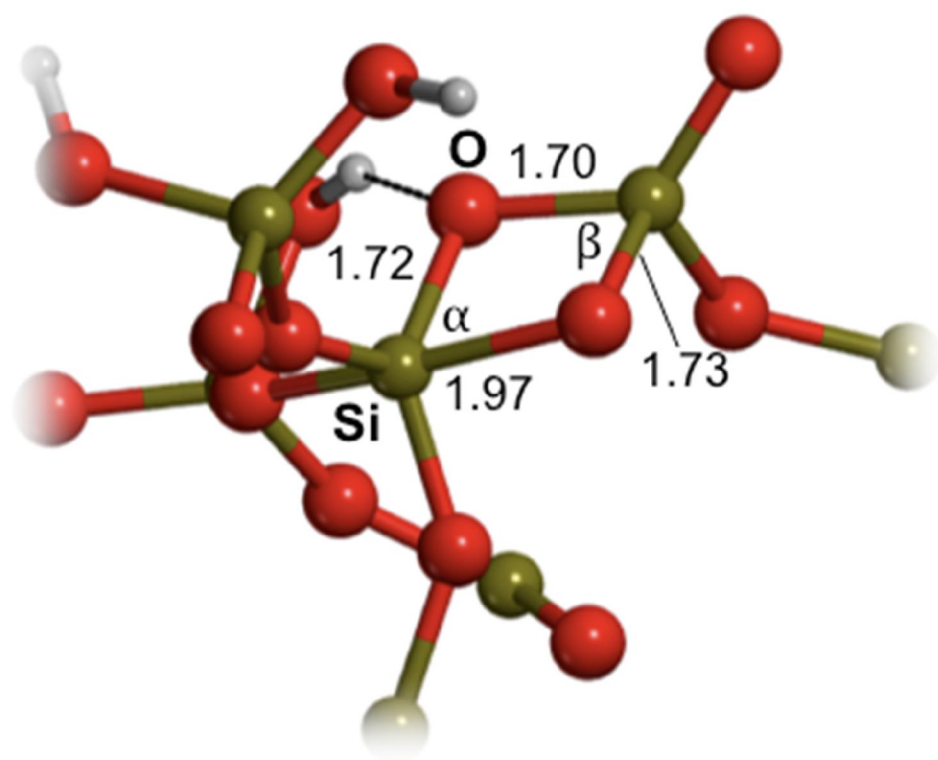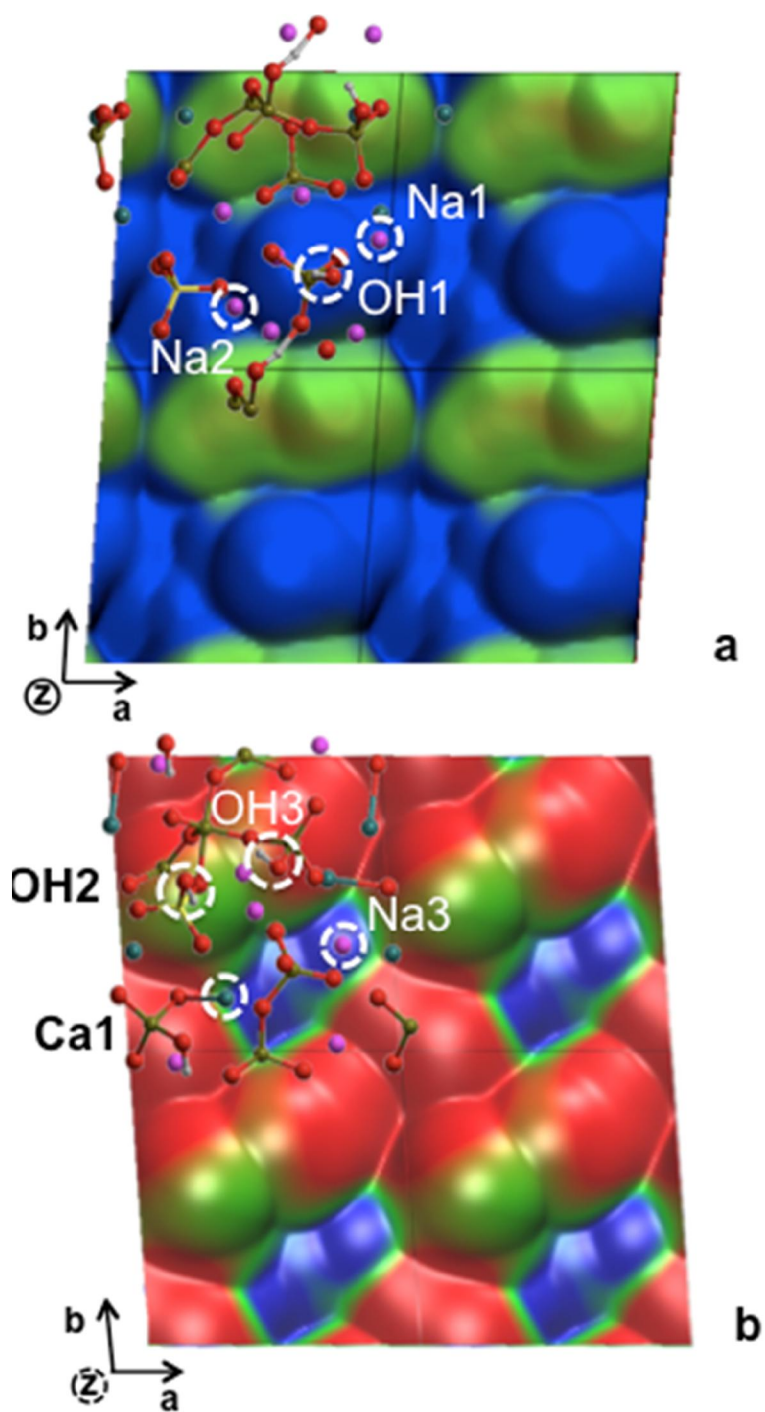**Figure 5.**
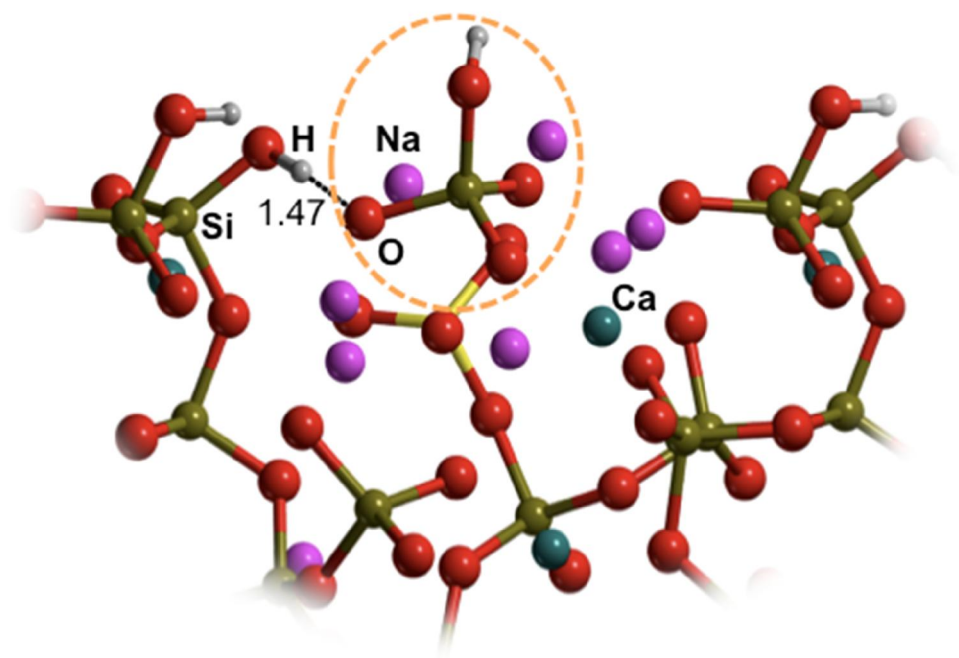
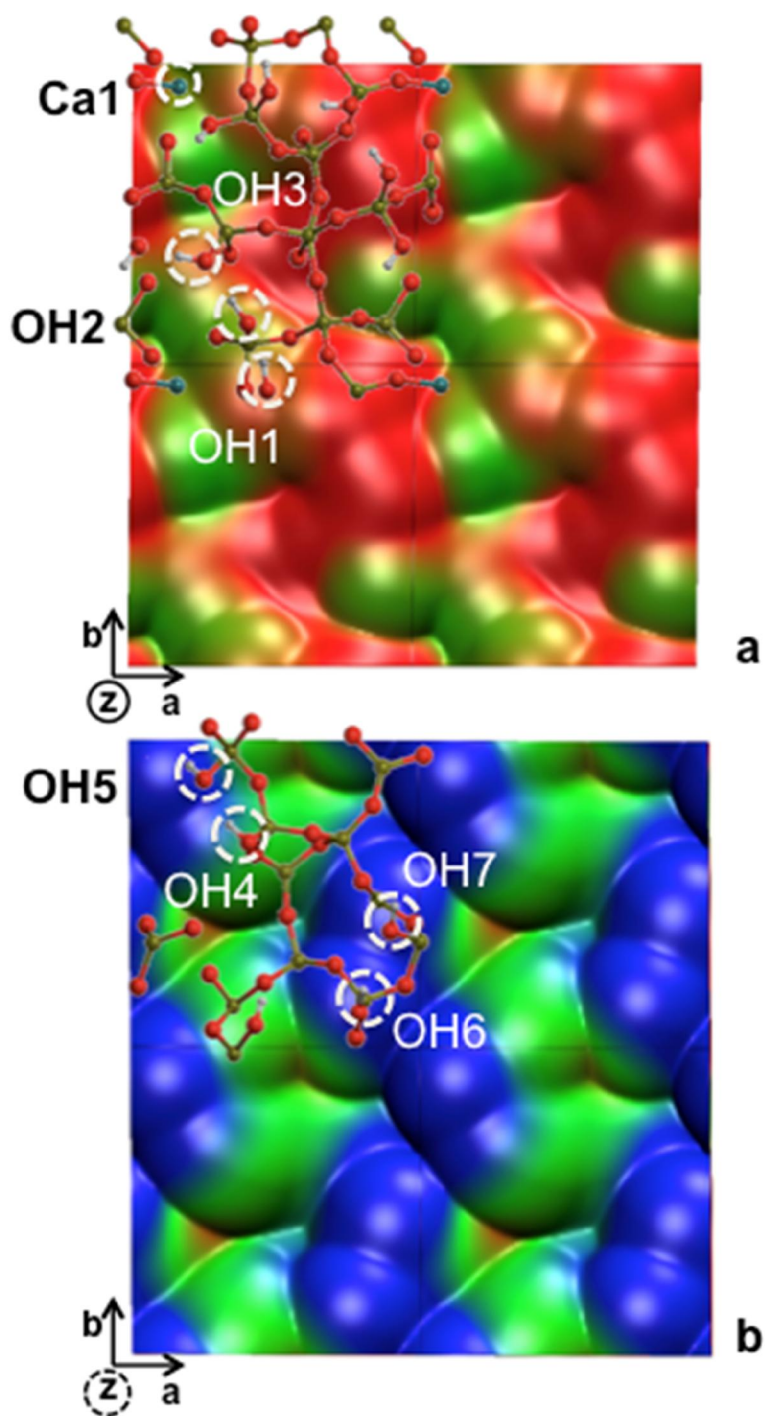**Figure 6.**

Figure 7.

Figure 8.

Figure 9.

Tables.

Table 1. Geometrical features (average values) of the relaxed *ab* surfaces of both glasses compared to the respective bulk ones. All distances are in Å and bond angles are in degrees.

	45S5		77S	
	Bulk	*ab*	Bulk	*ab*
Si-O	1.63	1.68	1.66	1.67
Si-NBO	1.62	1.64	1.62	1.63
Si-BO	1.69	1.70	1.66	1.68
P-O	1.57	1.60	1.57	1.58
P-NBO	1.56	1.57	1.51	1.57
P-BO	1.66	1.63	1.60	1.63
Na-O	2.39	2.38	---	---
Na-NBO	2.38	2.38	---	---
Na-BO	2.65	2.40	---	---
Ca-O	2.42	2.37	2.43	2.46
Ca-NBO	2.39	2.35	2.35	2.38
Ca-BO	2.60	2.52	2.65	2.66
O-H	---	1.07	---	0.98
Ω (O-Si-O)	109.3	108.9	109.4	109.1
Ω (O-P-O)	109.5	108.3	109.2	109.0
Ω (Si-O-Si)	131.3	133.2	142.6	132.1
Ω (P-O-Si)	123.0	133.3	135.2	132.8

Table 2. Main properties of the relaxed *ab, ac* and *bc* surfaces of the 45S5 and 77S bioglasses starting from the respective bulk structures (78 and 80 atoms for 45S5 and 77S, respectively). The total number n° of H_2O molecules needed to completely heal each surface is shown. The surface hydroxyl density ρ[OH] is considered as the average number of the OH groups on the upper and lower face of the slabs per unit of surface area. The thickness of the slab is measured as the difference of the z coordinates of the most exposed atom on the upper face and the most exposed one on the lower face. E_{form}/H_2O refers to the formation energy of the reconstructed surface per water molecule after equation 1 (see text).

Surface	45S5			77S		
	ab	*ac*	*bc*	*ab*	*ac*	*bc*
n° atoms	87	81	87	98	101	95
n° H_2O	3	1	3	6	7	5
ρ [OH nm^{-2}]	3.1	1.0	2.8	6.6	6.8	4.6
Thickness (Å)	13.07	10.84	12.59	12.34	12.56	14.81
μ_z (Debye)	2.303	-2.397	1.377	-2.443	1.390	-3.706
E_{form}(kJ/mol)/H_2O	172.0	458.4	124.5	-7.8	0.2	5.2

Table 3 Computed Qn distribution of silicon for all the surface models of the 45S5 and 77S bioglasses.

	Q0	Q1	Q2	Q3	Q4	Q5
45S5 *ab*	15.4	23.1	30.8	15.4	15.4	---
45S5 *ac*	---	15.4	61.5	7.7	15.4	---
45S5 *bc*	7.7	15.4	61.5	---	15.4	---
77S *ab*	---	---	33.3	33.3	33.3	---
77S *ac*	---	19.1	9.5	33.3	33.3	---
77S *bc*	---	---	19.1	38.1	38.1	4.8

Table 4. Concentration (Number Density/nm^3) of relevant sites in the top and bottom layers of the surface models of the 45S5 and 77S bioglasses. The thickness of the layers chosen is 3 Å. [§] For the 3 membered rings (3MR) the whole thickness of the surface model was taken in consideration for the density calculation.

Site	45S5			77S		
	ab	*ac*	*bc*	*ab*	*ac*	*bc*
Na$^+$	8.6	12.0	4.7	---	---	---
Ca^{2+}	1.7	3.4	3.1	1.6	3.2	0.0
NBO	15.6	30.8	15.7	6.3	8.1	7.6
2MR	---	---	---	---	1.6	1.5
3MR[§]	---	---	0.7	1.5	---	---

Table of Content Graphic